Toward an automated tool for dislocation density characterization in a scanning electron microscope

S. Cazottes, A. Bechis, C. Lafond, G. L'hôte, Tom Dreyfus, C. Roth, P. Steyer, Thierry Douillard, C. Langlois

Toward an automated tool for dislocation density characterization in a scanning electron microscope

S. Cazottes[a]*, A. Bechis[a], C. Lafond[a], G. L'Hôte[a], A. Roth[b], T. Dreyfus[b], P. Steyer[a], T. Douillard[a], C. Langlois[a]

[a] Univ Lyon, CNRS, INSA-Lyon, MATEIS UMR5510, F-69621 Villeurbanne, France

[b] RedantLabs, 19 rue du Père Chevrier, 69007 Lyon, France

(* corresponding author : sophie.cazottes@insa-lyon.fr; Tel 00 33 4 72 43 82 45, Fax 00 33 4 72 43 85 28)

Graphical abstract

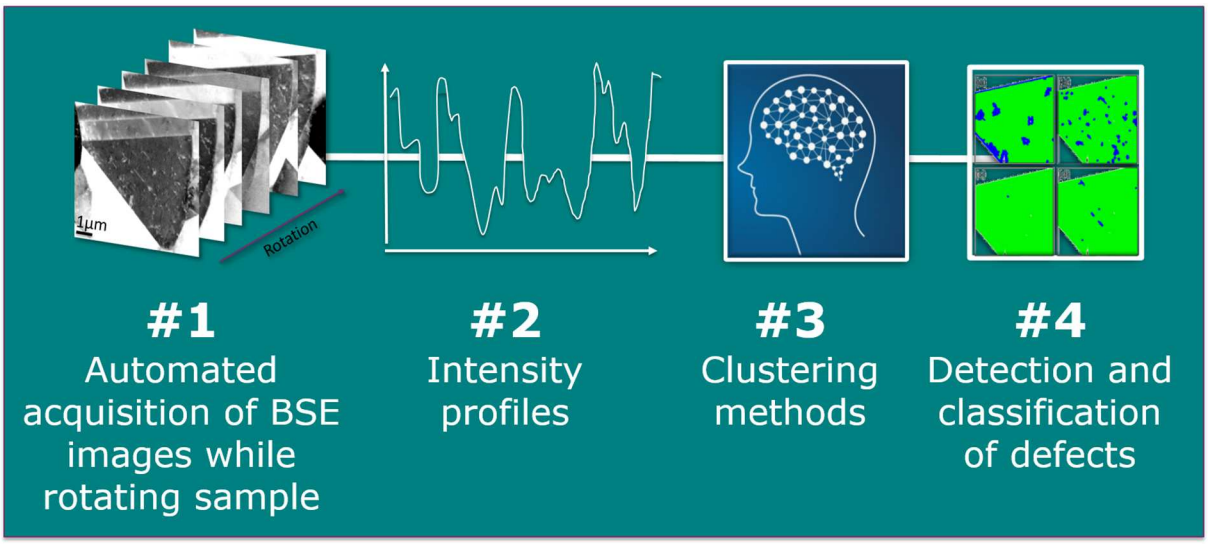

Keywords: Electron channeling contrast imaging; dislocations; scanning electron microscopy; data clustering

Abstract

We propose a methodology for quantitative dislocation characterization of a bulk sample in a scanning electron microscope without requiring pre-orientation of the sample before analysis. In this method, a series of backscattered electron images are acquired while rotating the sample, and an intensity profile as a function of the rotation angle is obtained for each pixel of the observed area. These intensity profiles are used to determine the orientation condition of the analyzed grain. The nature of the pixel is defined as what dominates the pixel intensity (matrix, defect or noise). As the intensity profiles are also characteristic of the pixel nature, a data clustering algorithm is applied to the intensity profiles to classify the pixel nature. As a result, the defect density, such as the dislocation density, can be automatically measured. The proposed method is fast and efficient compared with transmission electron microscopy analysis and could enable the future characterization of multiple grains in a deformed sample within a reasonable amount of time.

Introduction

During the past decade, considerable efforts have been devoted to the development of integrated modeling approaches covering material processing to the final material properties [1]. In these approaches, the microstructural parameters (*e.g.,* precipitate distribution, grain size) are calculated for a given thermo-mechanical process and used as input for modeling of the mechanical properties. However, a key parameter required for predicting the mechanical properties, the dislocation density, remains improperly and rarely predicted. There is thus a crucial need for accurate experimental measurement of the dislocation density.

Upon all methods available, dislocation density can be measured by transmission electron microscopy (TEM), electron channeling contrast imaging (ECCI), or by electron back scattered diffraction (EBSD). TEM allows a direct observation of dislocations with a very good spatial resolution. Therefore, individual dislocation can be relatively easily well resolved, so that relatively high dislocation densities can be characterized (~10^{15} m^{-2}) [2]. However, the observed area in TEM is quite limited, and in the case of low dislocation densities or heterogeneous microstructure, those measurement become time consuming. On the other

end, the development over the last two decades in EBSD detector sensibility and indexing speed allowed a fast development of the use of EBSD for the determination of geometrically necessary dislocation (GND) [3]. This method is particularly useful for high dislocation densities [4]. Its precision is however limited by the angular resolution and related to the step size used. Recently, the efficiency of electron channeling contrast imaging (ECCI) has been demonstrated for defect characterization of bulk samples in a scanning electron microscope using the channeling contrast of electrons [5-11]. It is now possible to characterize dislocation densities [5], the nature of dislocations [7], and the nature of stacking faults (SFs) for different types of materials. ECCI is particularly well adapted for heterogeneous microstructures as it allows large field of views. It is also widely used to characterize dislocation structure in fatigued materials [12-14] or specific dislocation/ microstructure interactions [15-16]. ECCI is particularly suitable for characterizing low dislocation densities. Indeed, for large dislocation density, dislocations will overlap, which makes the measurement impossible. Most of the studies on metallic materials present samples with dislocation densities lower than 1-5 x 10^{14} m^{-2}.

There are several available methods to measure the dislocation density of a grain [11,17,18]. All of these methods are based on counting the dislocations visible in the area of interest. The counting is often performed manually on individual images. The TEM and ECCI defect study is based on the $\vec{g}.\vec{b}$ method and the analysis of invisibility criteria [19] ($\vec{b}$ is the Burgers vector of the dislocation and $\vec{g}$ is the diffracting vector). Indeed, when the matrix is in a so-called "Two-Beam" condition, a single diffraction vector $\vec{g}$ is excited. If a small positive deviation from this orientation is introduced, the dislocation contrast becomes enhanced, the matrix appears dark, while dislocations appear white. In the case of a screw dislocation, if the product $\vec{g}.\vec{b} = 0$ the dislocation is invisible and if the product $\vec{g}.\vec{b} \neq 0$ then the dislocation is visible. In order to determine the Burgers vector of a screw dislocation, it is therefore necessary to observe it under different two – beam conditions. With at least two invisibility conditions, it is possible to determine its Burgers vector. The approach is similar for edge dislocations, with the following invisibility condition: $\vec{g}.\vec{b} \neq 0$ and $\vec{g}.\vec{b} \wedge \vec{u} \neq 0$. In the case of stacking faults, the extinction condition becomes $\vec{g}.\vec{R} \neq 0$ with $\vec{R}$ the translation vector induced by the presence of the defect. Note that in the case of ECCI observations, stress

relaxation occur on dislocations that and can modify the visibility/invisibility conditions for mixed dislocations [20].

Reliable characterization of the dislocation density and Burgers vector thus requires several measurements under different two beam conditions. As diffraction conditions are specific for each grain, this orientation procedure must be repeated for each analyzed grain. Consequently, TEM and/or ECCI observations are time consuming, and often, only a few grains are analyzed. The representativeness of such measurements is thus questionable. Furthermore, it is well known that the deformation state is orientation dependent, and a minimum number of grains with different orientation must be characterized.

This paper presents an alternative method for quantitative dislocation imaging and characterization based on the CHanneling ORientation Determination (CHORD) set-up that does not require any preliminar specific orientation of the sample. The CHORD technique utilizes a set of ion-induced secondary electron images (iCHORD)[21] or ECCI images (eCHORD) [22] to automatically map the crystallographic orientation of grains. For eCHORD, subsequently referred to CHORD, the sample is tilted with respect to the electron beam and then rotated 360°, with an image recorded for every rotation step. After alignment of the series of images, an intensity profile as a function of the rotation angle is obtained for each pixel of the area of interest. This intensity profile is an unequivocal signature of the orientation of the grain. Then, the crystallographic orientation of each pixel is deduced by comparison of this profile with a simulated electron channeling pattern (ECP). Indeed, an ECP represents the BSE intensity collected for different angles between the crystal and the electron beam [23-24]. The ECP are simulated from EMsoft simulation suite from M. De Graef *et al.* [25][26]. In our characterization approach, the CHORD procedure is used to identify the crystallographic orientation of the grain and to determine the orientation condition leading to dislocation observation. When the electron beam is located at the edge of a Kikuchi band, a two beam condition is reached [11], and the Bragg condition is fullfilled [24]. If a slight deviation from this Bragg orientation is applied, defects contrast can be maximized. For instance, if a positive deviation is applied, the matrix appears dark and dislocations appear with a bright contrast, which corresponds to a minimum in the intensity profile. The rotational-ECCI (R-ECCI) method involves the rapid acquisition of a 360° rotation image to obtain the intensity profile of the grain under study [13]. From the intensity profile,

the rotation angles corresponding to intensity minima are determined. The sample is then rotated to reach one of these two beam conditions and the dislocation structure can be imaged. The dislocation density can then be determined from such images. However, as only one two beam condition is considered, in which some dislocations may be in the extinction condition, the density measurement may be biased. That's why our procedure take into account several two beam conditions, leading to a more exhaustive approach of dislocation types.

Dislocation fields are generally determined using TEM characterization, which requires tedious sample preparation that can affect the dislocation structure and focuses on very small areas. Using scanning electron microscopy (SEM), the observed area is more representative of the material; that’s why we propose to automatically characterize and quantify defects by exploiting CHORD intensity profiles. Indeed, the intensity of defect and matrix pixels differs when the matrix is in the two beam condition. Direct determination of the pixel nature can thus eliminate the manual image processing step necessary for measurement of the dislocation density and characterization of the dislocation nature.

The aim of this paper is to present the possibilities and limits of using the intensity profiles, rather than images, to characterize dislocations in a scanning electron microscope. The complete acquisition procedure and the use of advanced clustering methods for the data treatment are presented. The results obtained for a duplex stainless steel are presented as an example, and the future potential of this procedure is discussed.

Experimental set-up

The experimental set-up used in this work is described in [22]. The specimens were mounted to a dedicated sub-stage placed in a classical scanning electron microscope goniometer to enable fast and precise control of the displacement and rotation (on the order of nanometers and microdegrees, respectively). The sub-stage was controlled using software developed by our group to enable automatic rotation–acquisition. Backscattered electron (BSE) images were automatically acquired for every rotation step of the sample using a standard bottom column BSE detector. A scan rotation correction was performed at each

acquisition to ensure that the exact same region of interest was examined for each acquisition step.

The observation conditions were those typically used for ECCI (Zaefferer and Elhami, 2014). Serial imaging was performed using a Gemini I SEM column (Carl Zeiss Microscopy GmbH, Oberkochen, Germany) equipped with a retractable standard four-quadrant solid-state detector (4Q-BSD). The accelerating voltage was set to 20 kV, the aperture size was 120 µm, and the so-called high-current mode was activated. A tilt angle value of 10° and a WD of 7mm were chosen, as in Lafond *and al* work [22]. For this set-up, the beam current is estimated to be around 10nA [11]. Two images series were recorded with an image size of 1024 x 768 pixel: the first one, at low magnification (pixel size = 22.3 nm), and with a fast scan speed (dwell time = 1.74 ms – 1.4sec/frame), and the second one at higher magnification (pixel size = 5.6 nm) and a slower scan speed (dwell time = 26.32ms – 20sec/frame).

The sample studied was as-received commercial 2101 lean duplex stainless steel from Outokumpo; the microstructure of the sample is shown elsewhere [27]. The sample was prepared by mechanical polishing down to 1 µm followed by a vibratory polishing step using a colloidal-type suspension. This material was selected because of its small grain size (5–10 µm). As the sample is undeformed, its dislocation density is expected to be quite small, around 10^{12} to 10^{13} m^{-2}.

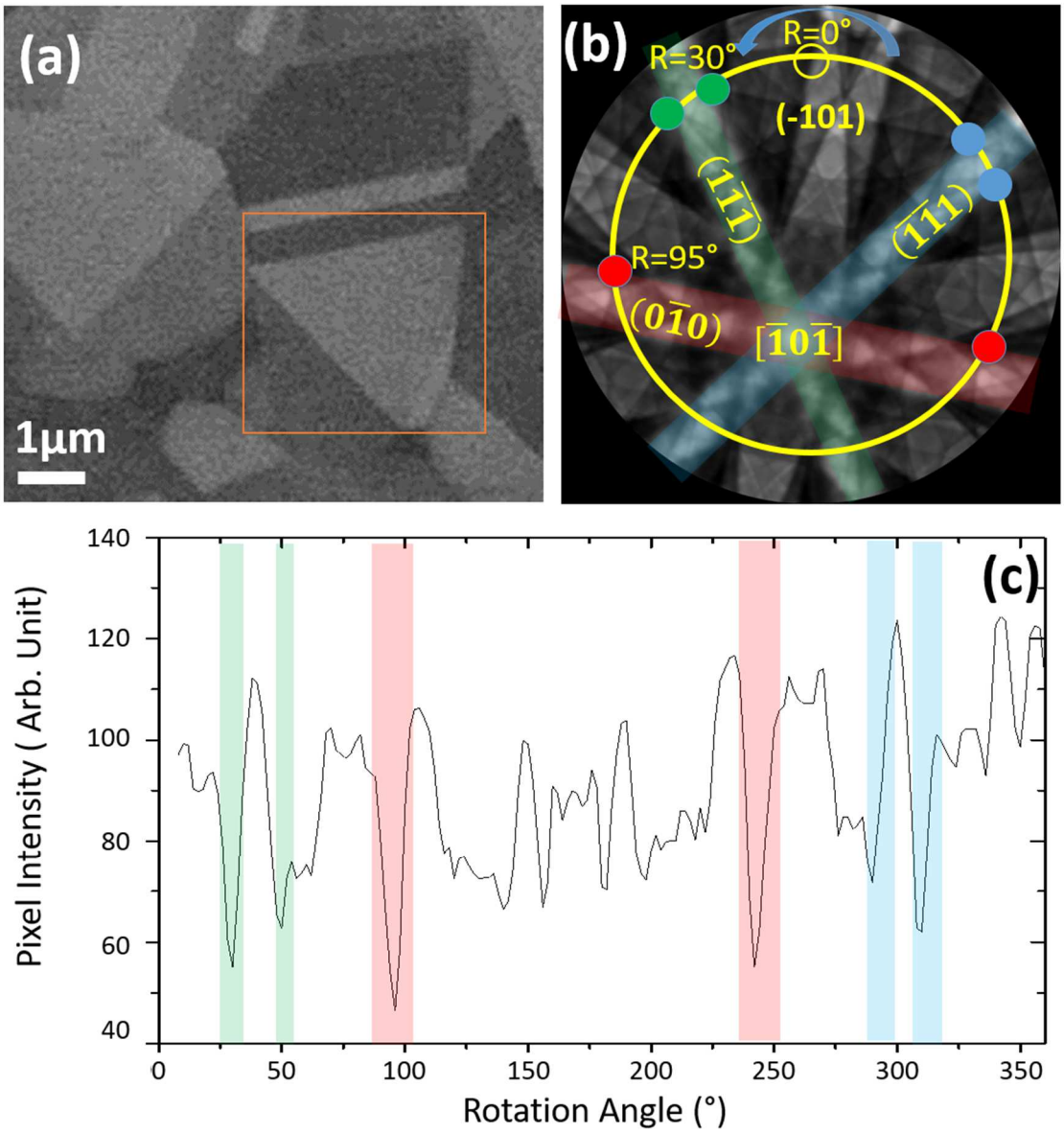

Figure 1: Fast CHORD image series recorded for the ROI; rotation step = 2°, tilt = 10°, pixel size - 22.3 nm, and accelerating voltage = 20 kV. (a) One of the collected BSE images, (b) calculated ECP of the selected grain using EMSoft [25][26], and (c) corresponding experimental intensity profile. At a sample rotation angle of 30° and 50°, the $(1\bar{1}\bar{1})$ *band is crossed, while the* $(0\bar{1}0)$ *band is crossed for R=95° and R=245°. The* $(\bar{1}\bar{1}1)$ *band is crossed for R=390° and R=315°.*

The first step of the procedure consists of acquiring a fast CHORD image series of the region of interest (ROI). After image alignment, an intensity profile as a function of the

rotation angle is available for each pixel of the ROI. From this profile, the grain orientation is deduced (see [22] for additional details).

Figure 1a presents a BSE image of a ROI as an example; the white triangular grain was selected for dislocation imaging. The rotation series of this ROI was acquired in less than 5 min using the protocol described in [22]. The intensity profile of the whole selected grain is shown in Figure 1c. The intensity profile was correlated to the ECP presented in Figure 1b, where the yellow circle represents the electron beam path followed during the 360° sample rotation with a tilt angle of 10°. It is apparent that this path crosses different Kikuchi bands such as the $(1\bar{1}\bar{1})$ band at a rotation angle of about 30° and the $(0\bar{1}0)$ band at a rotation angle of about 95°. The intensity profile present a minimum close to those particular rotation angles, which corresponds to the optimum orientation for dislocation imaging, where the matrix will appear dark and dislocations bright. Therefore, to visualize dislocations, the rotation angles needed to reach those maximum contrasts orientation can be directly read on the intensity profile at the rotation angles corresponding to minimum values. This process can be used to rapidly find suitable conditions under which some dislocations are visible, without requiring any electron backscatter diffraction analysis or pre-orientation of the sample. This approach is thus rapid and allows a first imaging of the dislocation structure [13].

However, to quantitatively measure the dislocation density or to determine the Burgers vector of the present dislocations, imaging under more than one two beam condition is necessary. By acquiring images for all the rotation angles, *i.e.,* 360 images, many two beam conditions are assumed to be reached, which should allow quantitative dislocation density measurement as well as **g.b** analysis. However, practically, a low scan speed (30 s to 2 min acquisition per frame) is required to visualize the dislocations in the ECCI images of the series. The total acquisition time is thus very long and may lead to sample drift and loss of focus over time. Moreover, because of the high magnification required (pixel size < 5–10 nm), a fully automatic procedure is not yet possible as scanning instabilities causes images distortion. Therefore, a semi-automatic procedure was preferred: the interesting two beam conditions were determined from the intensity profile (six conditions for that particular grain), and mini-rotation series were acquired around those conditions. For each mini-rotation series, a rotation step of 0.5° was used with the total rotation angle varying from 5° to 10° (see Figure 2). The acquisition speed for all the images was 30 s/image, which is quite fast for ECCI, and

the magnification was 20kX (pixel size = 5.6 nm). The observed dislocation width was 20-25 nm, which corresponds to 4 or 5 pixels.

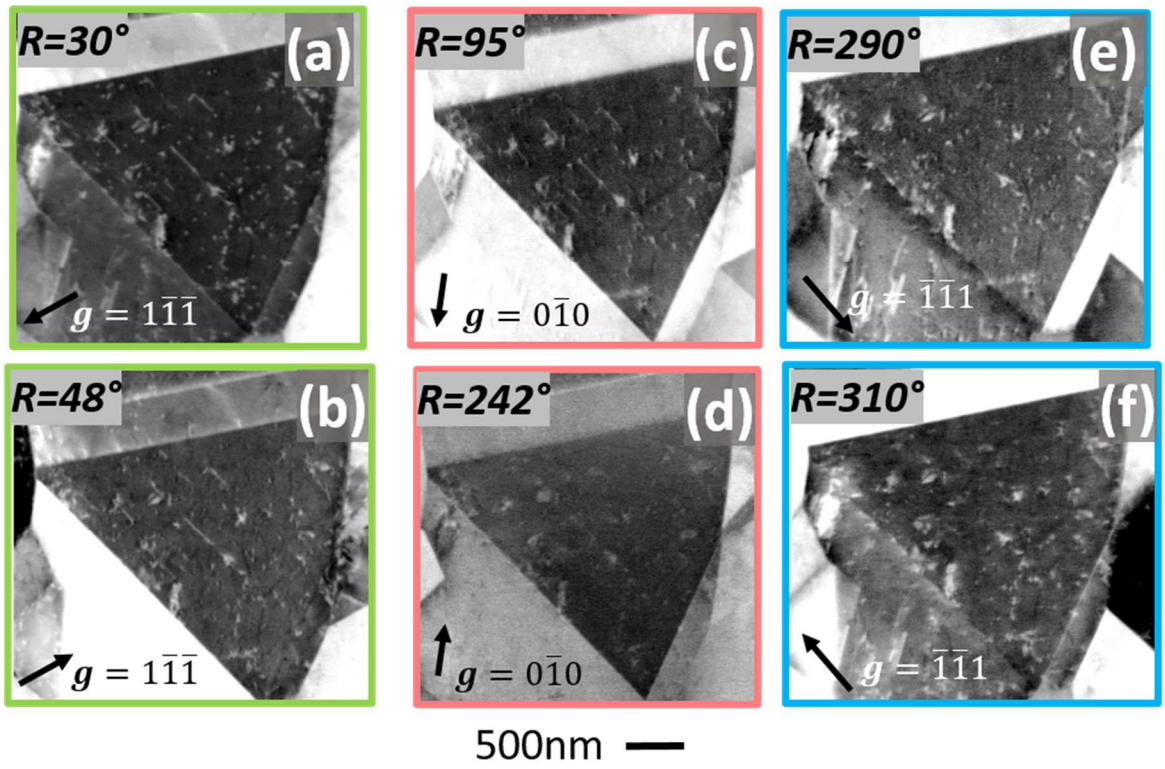

Figure 2: (a)–(f) Sum images from the mini-series (over four images centered on the best diffraction condition – total rotation angle of 2°) for the six two beam conditions selected.

Results

1. Intensity profiles as defect markers

Figure 2 shows the dislocation structure for all the selected rotation angles. Most dislocations were visible for the $\boldsymbol{g} = 1\bar{1}\bar{1}$ condition, with some dislocations disappearing for the $\boldsymbol{g} = \bar{1}\bar{1}1$ and $\boldsymbol{g} = 0\bar{1}0$ conditions.

The use of the intensity profiles to automatically detect the different defects instead of independent ECCI images was then considered. All the mini-series images were gathered to create a new stack of images. Then, the stack was aligned in Fiji software using affine transformations. The complete alignment procedure is detailed in [22]. Thanks to the use of a

rotation correction during image acquisition, a precise enough alignment can be achieved, considering the pixel size (5.8nm). Therefore, an intensity profile as a function of the image number was generated for each pixel. As an example, Figure 3 presents parts of the complete intensity profile corresponding to the $\boldsymbol{g} = 1\bar{1}\bar{1}$, $\boldsymbol{g} = 0\bar{1}0$, and $\boldsymbol{g} = \bar{1}\bar{1}1$ conditions for the matrix and for two selected dislocations.

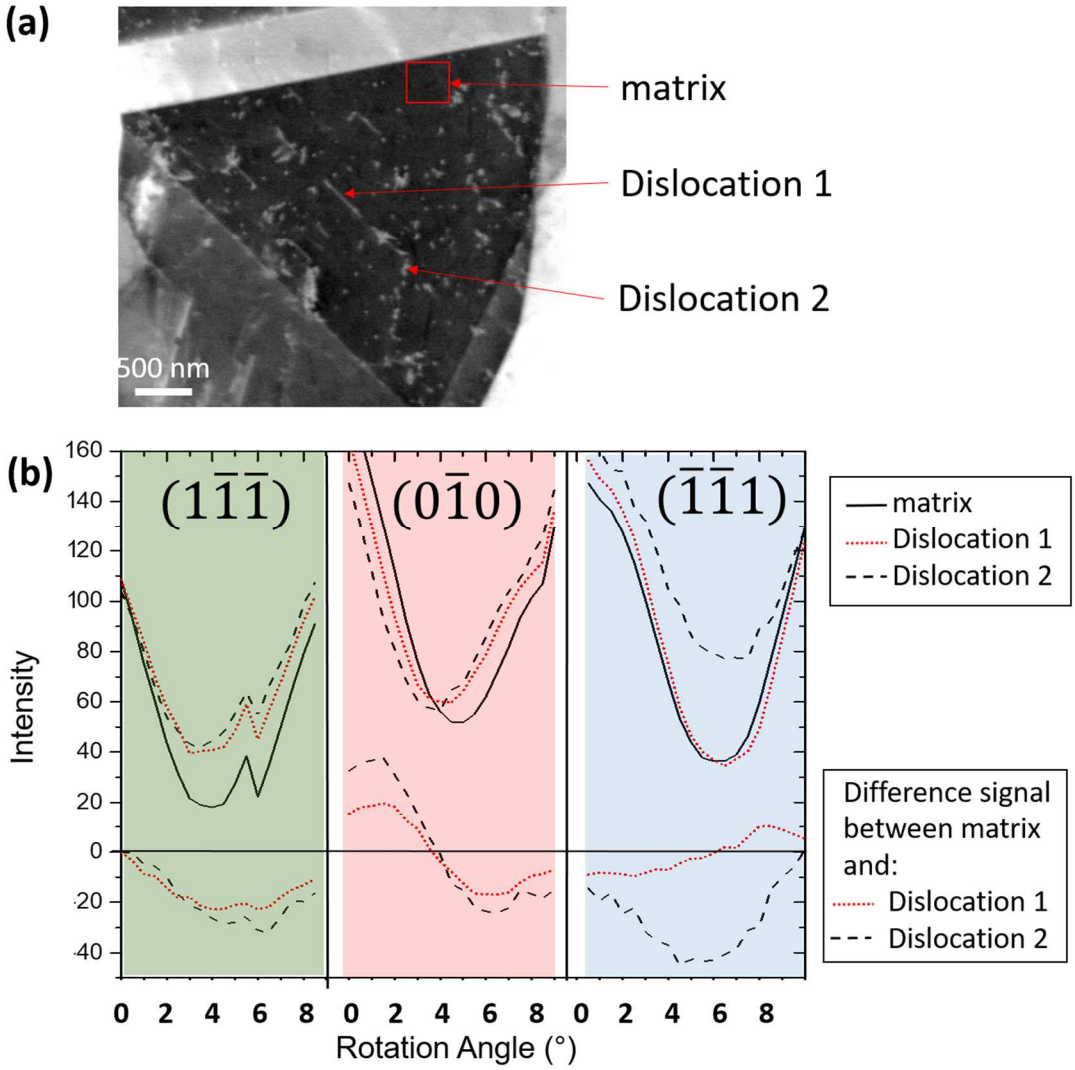

Figure 3: (a) Selection of the matrix pixels (red square) and of pixels of two different dislocations to generate corresponding intensity profiles (b). The difference signal between the matrix and defects are also presented at the bottom.

The intensity profiles of the matrix and of the dislocations close to the three two beam conditions were similar to those calculated in [11]. The signal differences between the matrix and the selected dislocations are also shown in Figure 3. The matrix pixels are the one located

inside the red square, while a couple of pixels located at the position of the red arrays were selected for the two dislocations. The intensity difference of the dislocation signal was approximately 20%–40% of the matrix intensity, which is more than sufficient to efficiently discriminate pixels attributed to the matrix from those attributed to dislocations. It is worth noting that the maximum intensity difference appeared at the minimum contrast condition of the matrix, as expected from ECCI theory [11], as observed for the $\boldsymbol{g} = \bar{1}\bar{1}1$ condition. This is however not so clear for the $\boldsymbol{g} = 1\bar{1}\bar{1}$ condition where the signal difference is maximum and constant over 2edgrees around the minimum contrast condition. This result indicates that the dislocations are visible for a relatively large angular spread (more than 5° in this case), which could result from the crystallographic path followed during the rotation. The beam crosses the $\boldsymbol{g} = (\bar{1}\bar{1}1)$ plane almost perpendicularly, whereas the $\boldsymbol{g} = (1\bar{1}\bar{1})$ plane is crossed with an incident angle close to 10°. Therefore, the minimum contrast condition for the $\boldsymbol{g} = (1\bar{1}\bar{1})$ plane and the difference signal are more angularly spread as a function of the rotation angle. For the $\boldsymbol{g} = (\bar{1}\bar{1}1)$ condition, the intensity profile of the dislocation 1 is well superimposed with the one of the matrix. This finding is consistent with the fact that dislocation 1 was not visible in the images for that diffracting condition. Dislocation 2 signal present a similar profile as the matrix, but the intensity of its minimum is different: dislocation 2 is visible in that diffraction condition. For the $\boldsymbol{g} = (0\bar{1}0)$ diffracting condition, the intensity signal of dislocation1 and of dislocation 2 are almost superimposed with that of the matrix, even if a slight shift in the peak is observed. This similarity resulted in a difference signal with an intensity of less than 5% and a flat shape, indicating that the dislocations are extinguished for this rotation angle, although a slight contrast is visible in the image. When a dislocation appears in a TEM or ECCI image, a residual contrast is often observed even if the defect is in a so-called extinction condition, which can lead to an incorrect interpretation of the extinction condition. The signal difference shape of the intensity profile provides a quantitative tool to distinguish between extinction or visibility conditions. This example proves that intensity profiles can be of great assistance in identifying matrix and dislocation pixels and in classifying defects by their nature, as explained in the following section.

2. Clustering method for defect detection

The proposed clustering method for defect detection consists of two main steps: first, the different grains are separated, and then, the defects in each grain are detected and characterized. The process is summarized in Figure 4.

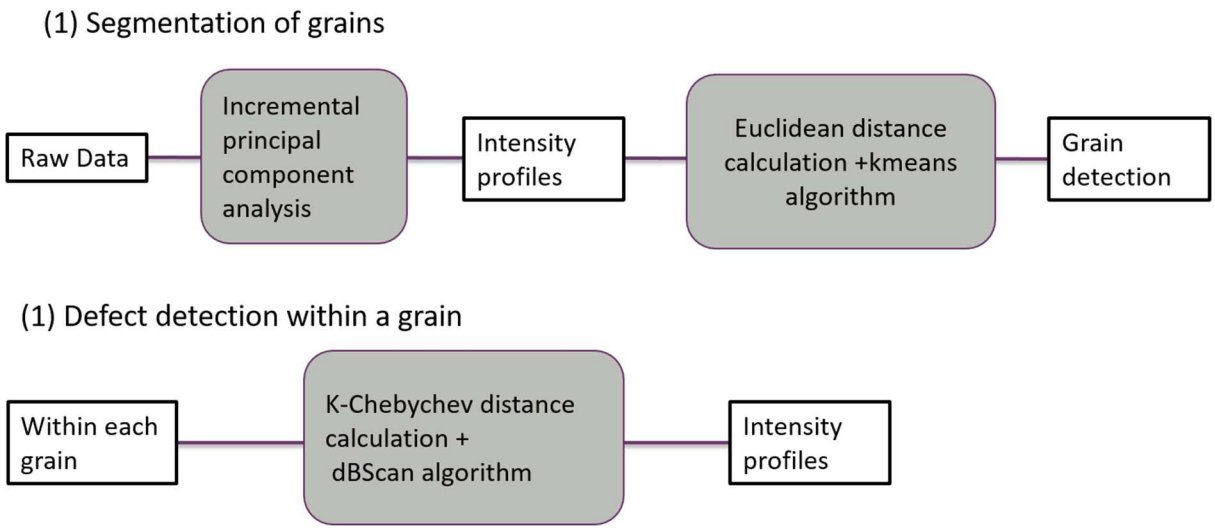

Figure 4: Image analysis process.

2.1 Segmentation of grains

The initial data are represented by the set of intensity profiles for every pixel in the images. The profile associated with a (X,Y) coordinate is a N-dimensional vector, where N is the number of images. The clustering method is based on the calculation of the distance in the N-space between all intensity profiles.

A data set contains up to 360 images, each of which contains up to 3 million pixels. Therefore, running the clustering over the entire data set might require the processing of more than 4GB of data. However, some information is highly redundant in the profiles over a grain. Thus, to reduce the size of the data requiring processing, a principal component analysis (PCA) is used. A PCA projects the data onto a lowered dimensional space. In this case, an approximation of the PCA, the incremental PCA, was preferred [28]. It allows the principal component to be built incrementally using batches of a given size and reduces the memory needed to build the PCA. Once the size of the data was reduced, clustering was performed

using a k-means algorithm that makes use of a kd-tree representation of the data points and the Euclidean distance as a metric [29].

Once the cluster was calculated, post-processing operations were performed to merge or split undesirable clusters. As a result, the grain analysis was efficient when the number of grains was small, which is suitable for the high magnifications required for dislocation imaging.

2.2 Defect detection within a grain

The next step of the procedure consists of labeling each profile within a selected grain. Three labels were selected: defect, matrix, and noise. Matrix pixels correspond to all the positions (X,Y) in the analyzed stack that shared similar profiles along all dimensions. Defect profiles present dissimilarities compared with the average matrix profile only on a series of consecutive dimensions. Noise profiles are either flat profiles or profiles that do not fit into the other two categories. The number of defects present within a grain is undetermined before the clustering process; therefore, a non-knowledge-based algorithm is required.

The following clustering procedure was applied: first, a similarity score between profiles, $d_{kC}(p, p')$, was calculated. Provided a span parameter *k,* this score is given by the maximal cumulative difference in the intensity spread over *k* consecutive degrees. A defect differs the most from the matrix on a window of consecutive dimensions; therefore, it is more appropriate to use a variant of the Chebychev distance, where averages of the coordinates over consecutive dimensions are used rather than the direct use of the coordinates.

$$d_{kC}(p, p') = \max_{1 \le i \le n-k} \left| \frac{1}{k} \sum_{j=i}^{i+k-1} p_j - \frac{1}{k} \sum_{j=i}^{i+k-1} {p'}_j \right| \quad (1)$$

Here, *k* is the window size; d_{kC} is the k-window Chebychev distance, where *k= 1* is the usual Chebychev distance; *p* and *p'* are two different profiles; and *n* is the dimension of the intensity profile, which coincides with the number of images considered.

Note that we can replace each profile *p* by a profile

$$x_k = \left(\frac{1}{k} \sum_{j=0}^{k-1} p_j , \dots , \frac{1}{k} \sum_{j=n-k}^{n-1} p_j \right).$$

(2)

This means that the k-window Chebychev distance between two profiles (p, p'), $d_{kC}(p, p')$, is equivalent to the Chebychev distance $d_C(p_k, p'_k)$. A kD-tree representation can thus be used together with a clustering algorithm optimized for the Chebychev distance. This is the case for the *dbscan* cluster algorithm [30], which is a non-knowledge-based and fast algorithm. After labeling, the largest cluster is then considered to be the matrix, and the defects are classified depending on the angle at which the difference is calculated. Defects are thus classified from their visibility conditions.

As the clustering is performed on the profiles and not using the (X,Y) coordinates, it is possible for several features to be engulfed in the same cluster. For post-processing, to separate defect clusters that are not adjacent in the images, the connected components of the (X,Y) positions were computed for each cluster of profiles that was not labeled matrix. Small, connected components were discarded as noise, and for the rest, each profile was compared with the matrix average profile. If the difference was large enough, the profile was set as part of the feature; otherwise, it was considered as noise. The difference value was set as a variable parameter, adjusted by the user.

3. Application on a polycrystalline duplex steel: dislocation density measurements

The mini-series of images were analyzed using the clustering method described above. In the ROI, three different grains were detected, corresponding to three clusters (Figure 5a). Note that some features, indicated by the yellow arrows in Figure 5, were not included in the green grain. These features exhibited high contrast and were visible in all the images, even far away angularly from the Bragg condition. Recording a 360° image series would be necessary to determine if those features are topographical defects or dislocation type defects. Then, within each grain of interest, defect detection was performed (Figure 5b). The pixels were classified by type (matrix, defect, or noise), and the angles for which the contrast between the matrix and defect differed were determined. These angles correspond to the visibility conditions.

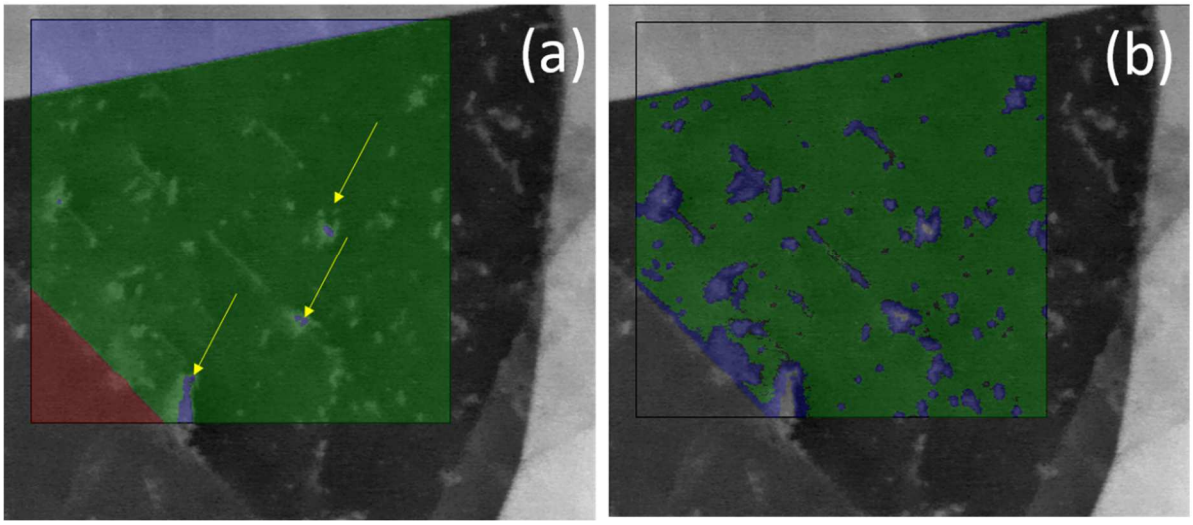

Figure 5: (a) Clustering of the mini-series used to detect the different grains (clusters) and (b) defect detection within the selected cluster.

4. Determining the defect nature

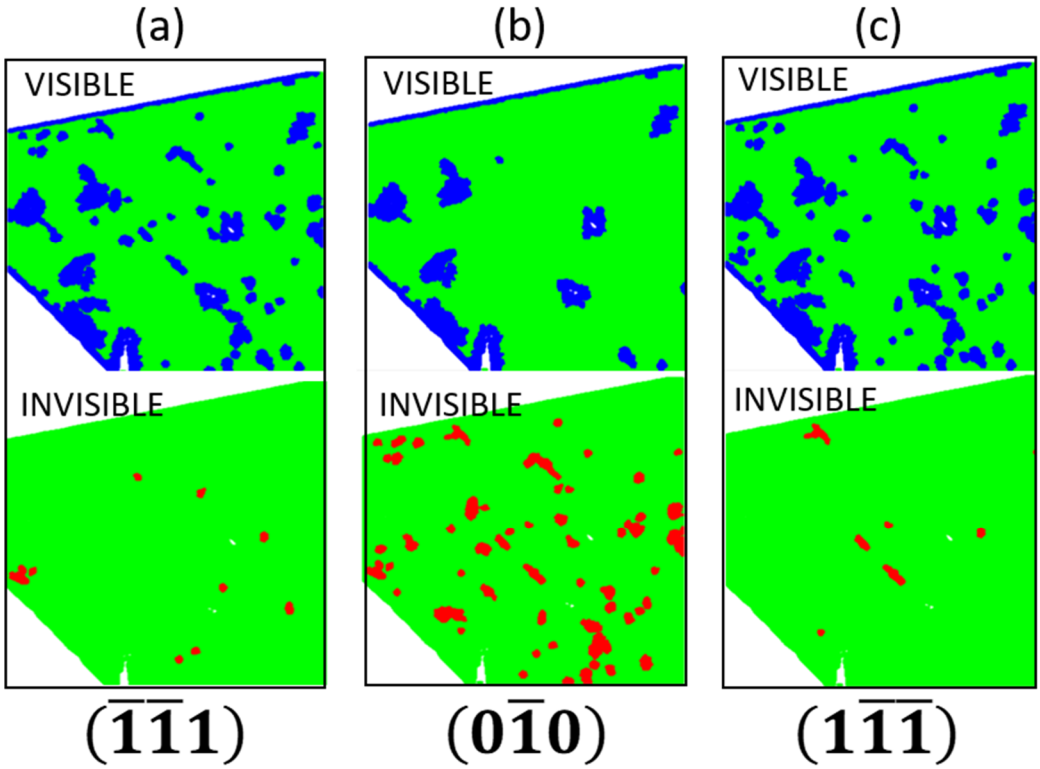

Figure 6: Visible (blue) and invisible (red) defects for the three diffracting conditions.

All the defects were classified from their visibility/invisibility criterion. In the example of Figure 6, the visible defects are shown in blue and the invisible defects are shown in red for the three diffracting conditions. This type of representation enables a direct comparison of the feature detection and original images. For this grain, the highest number of defects are visible for $\boldsymbol{g} = \bar{1}\bar{1}1$, in the image series as well as after profile analysis. Moreover, many dislocations are not seen in the $\boldsymbol{g} = 0\bar{1}0$, and this invisibility criterion is evidenced after the profile analysis, as can be seen of Figure 6b.

These visibility/invisibility conditions were used to determine the nature of the different defects. For a dislocation, knowing two conditions (two values of **g**) for which the dislocations are invisible (i.e., **g.b=0**) enables determination of the Burgers vector. In this particular example, the dislocations were classified depending on their visibility conditions.

In austenitic steel, the Burgers vector of the dislocations are expected to be of type $\vec{b} = \frac{1}{2} < 110 >$. Table 1 presents, for the different possible Burgers vector, the visibility/invisibility conditions and the corresponding dislocations observed. Most observed dislocations present a Burgers vector of type $\vec{b} = \frac{1}{2}[10\bar{1}]$, as it was visible for the $g = 1\bar{1}\bar{1}$ and for the $g = \bar{1}\bar{1}1$ condition. This is in good agreement with the images presented on Figure 2, for dislocations appearing as dots, *i.e*, perpendicular to the surface. No dislocations with Burgers vector of type $\vec{b} = \frac{1}{2}[110]$ or $\vec{b} = \frac{1}{2}[01\bar{1}]$ were found. One dislocation presents visibility/invisibility conditions that corresponds to a Burgers vector of type $\vec{b} = \frac{1}{2}[1\bar{1}0]$ or of type $\vec{b} = \frac{1}{2}[011]$. Line dislocations, *i.e.* that are not perpendicular to the surface, were detected to be visible only for the $g = 1\bar{1}\bar{1}$ condition, which do not corresponds to any expected Burgers vector in the fcc system. In this case, the visibility of those dislocations in the $g = 0\bar{1}0$ condition is questionable. Indeed, the line dislocations are visible on Figure 2c but not on Figure 2d. This can be related to the crystallographic path followed during the rotation series. The $g = 0\bar{1}0$ Kikuchi band is crossed relatively closed to the Zone Axis, and some other higher indices planes might be crossed simultaneously that affects the contrast between the defects and the matrix.

	$\frac{1}{2}[101]$	$\frac{1}{2}[10\bar{1}]$	$\frac{1}{2}[110]$ or $\frac{1}{2}[01\bar{1}]$	$\frac{1}{2}[1\bar{1}0]$ or $\frac{1}{2}[011]$	Other Burgers vector
$\boldsymbol{g} = \bar{1}\bar{1}1$	I	V	V	I	V
$\boldsymbol{g} = 0\bar{1}0$	I	I	V	V	I
$\boldsymbol{g} = 1\bar{1}\bar{1}$	I	V	I	V	I
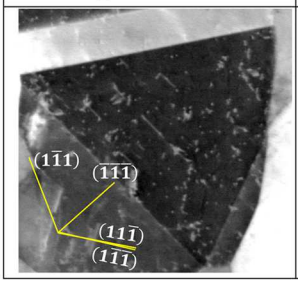		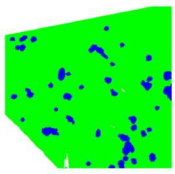	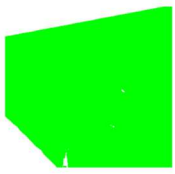	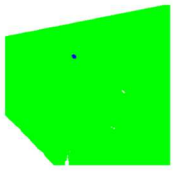	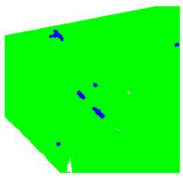

Table 1 : Analysis of invisibility/visibility criteria.

Once the defects were detected, the dislocation density was estimated using different methods. First, the density was estimated using a simple count method: $\rho = {}^{N}/_{S}$, where N is the number of defects and *S* is the analyzed area. Compared to the intercept method [17-18], or a 3D analysis using $\rho = {}^{L}/_{S.t}$ (with t the analyzed thickness [11], *L* the total dislocation line and *S* the surface of the grain), this 2D counting method has the advantage not be affected by the uncertainty in the thickness of the analyzed volume nor by the appearing dislocation width. Moreover, the results are not dependent on the orientation of the dislocation relatively to the sample surface. The simple count method was performed manually on the images corresponding to the three diffracting conditions, whereas the number of detected dislocations from the clustering method were used to calculate the '*clustering from profile*' value. A dislocation density of $(3.0 \pm 0.2) \times 10^{13} m^{-2}$ was estimated using the number of detected dislocations from the clustering method. It can be compared with the values obtained from a manual treatment on the images corresponding to the three diffracting conditions. For the $\mathbf{g} = \bar{1}\bar{1}1$ condition, a rather similar value was measured directly on the image: $(3.2 \pm 0.2) \times 10^{13} m^{-2}$, while lower values were obtained for the $\boldsymbol{g} = 0\bar{1}0$ condition $(2.0 \pm 20.2) \times 10^{13} m^{-2}$, and for the $\boldsymbol{g} = 1\bar{1}\bar{1}$ condition $(2.2 \pm 0.5) \times 10^{13} m^{-2}$ (see Figure 7). This is due to the fact that most dislocations are visible for the $\mathbf{g} = \bar{1}\bar{1}1$ condition and are not visible for the two other conditions. Such a quite small dislocation density is in the range of what can be expected for this type of steel in its as-received condition [31].

In the present example, most of the dislocations were visible for the $\boldsymbol{g} = \bar{1}\bar{1}1$ condition, whereas some of them disappeared for the $\boldsymbol{g} = 0\bar{1}0$ and $\mathbf{g} = \bar{1}\bar{1}1$ conditions. This result indicates that measurement of the dislocation density from a single image can lead to an error up to a factor of 2, highlighting the key-importance to consider several two beam conditions for a reliable dislocation density measurements, which is a tedious procedure when performed on single images. Moreover, orientation of the specimen is required for each two beam condition. When using a rotated image series, several two beam conditions can be rapidly accessed at the same time. The direct analysis of the intensity profile rises similar issues as manual image analysis for the evaluation of dislocation density. When dislocation overlap, such as in the case of highly deformed samples($\rho > 10^{15} m^{-2}$), the measurements will be biased. However, compared to a manual count, this method is fast and efficient since no preliminar orientation of the sample is required.

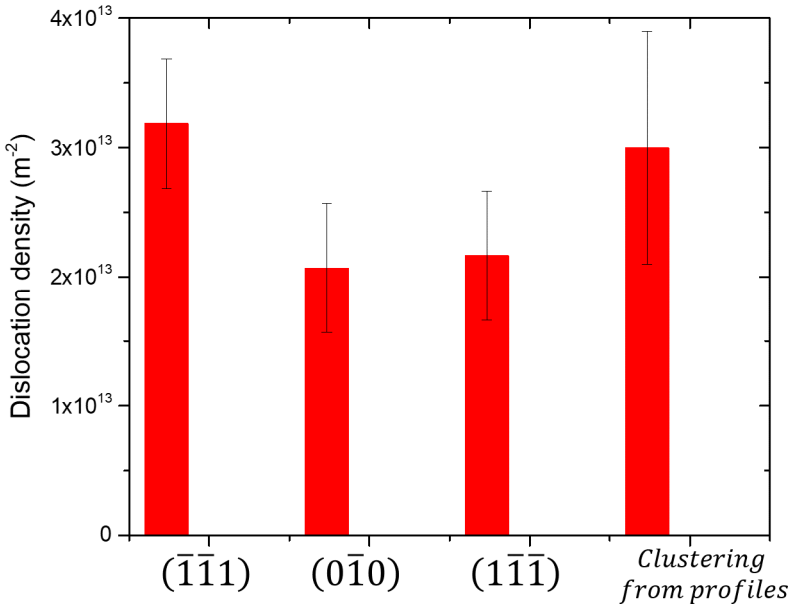

Figure 7: Comparison of dislocation density measurements from single image analysis and clustering method analysis. A surface analysis using the simple count was performed and compared with a 3D analysis.

Discussion

The proposed methodology enables semi-automatic and quantitative dislocation characterization, enabling efficient and fast dislocation density measurement, as the

measurements are simultaneously performed for several diffraction conditions. Moreover, the nature of the defects (Burgers vector, etc.) can be determined using a clustering procedure based on their visible/invisible criterion. The spatial resolution is that of the ECCI method, *i.e.,* 10–20 nm [11]. The classification of defects by type is beneficial for obtaining a better understanding of the mechanical properties of metallic materials as well as for the prediction of their mechanical behavior using constitutive laws.

This methodology was tested on a material presenting a small dislocation density (10^{13} m^{-2}), and therefore with grains that present almost no disorientation. Thus, the mean intensity profile of the matrix is the same whatever the position chosen in the grain. In the case of deformed samples, two problems might be encountered: the first one could be that the grain will present a disorientation leading to a variation in the mean intensity profile depending on the area selected. In that case, the data treatment should be adapted, and one solution could be to compare the intensity profile of a given pixel with the mean intensity profile around that given pixel. The second problem could be that, if the dislocation density is too high, dislocations will overlap on the images, making the measurement impossible, as for conventional ECCI image analysis. Therefore, this methodology is to date rather devoted to materials with dislocation density less than 1-5 x 10^{-14} m^{-2}.

Another limitation of the technique is that the crystallographic path cannot yet be selected. The methodology relies on a sufficient number of Kikuchi bands being crossed during the rotation. The crystallographic path depends mainly on two parameters: the accelerating voltage and tilt angle of the specimen. The accelerating voltage is selected to optimize the dislocation contrast; therefore, only the tilt of the sample can be adjusted. A statistical study is currently ongoing to determine the number of Kikuchi bands crossed for a random orientation. If, for a random orientation, the number of Kikuchi bands crossed is not sufficient, the development of a specific double tilt goniometer could allow more diffraction conditions to be accessed for the same grain.

Finally, the methodology is very dependent on the quality of the recorded image series. Important image drifts occurred during scanning at high magnification, which is required for dislocation imaging. Although some of the drift can be corrected by image analysis, more stable scanning systems are needed for further development of this method.

Distortion correction of the image using post-treatment methods could also limit the observed distortion.

Conclusion

In this work, a new approach for measuring the dislocation density based on the CHORD method was presented. The methodology consists of acquiring a series of BSE images while rotating the sample under suitable conditions for dislocation imaging. After alignment of the entire image series, an intensity profile, which is a signature for the crystallographic orientation, is obtained for each pixel. For each two beam condition, if a defect is visible, the intensity of the pixels corresponding to this defect will differ from that of the matrix. Using a dedicated clustering algorithm, visibility and invisibility criteria are analyzed to determine the nature of each pixel (dislocation, noise or matrix). Subsequently, quantitative measurement of the dislocation density is possible, and the quantitative parameters of the defects (*e.g.,* the Burgers vector) can be deduced. This procedure can be applied regardless of the orientation of the considered grain. As the proposed method is fast and efficient, it enables the characterization of large representative areas through the realization of several series of rotation within the same sample.

In the future, this method could be applied for the simultaneous characterization of several grains of deformed alloys in a single step.

Data availability

The raw/processed data will be made available on request.

References

[1] Bardel, D., Fontaine, M., Chaise, T., Perez, M., Nelias, D., Bourlier, F., Garnier, J., 2016. Integrated modelling of a 6061-T6 weld joint: From microstructure to mechanical properties. Acta Mater. 117, 81–90. https://doi.org/10.1016/j.actamat.2016.06.017

[2] Morito, S., Nishikawa, J., Maki, T., 2003. Dislocation Density within Lath Martensite in Fe-C and Fe-Ni Alloys. ISIJ Int. 43, 1475–1477. https://doi.org/10.2355/isijinternational.43.1475

[3] Pantleon, W., 2008. Resolving the geometrically necessary dislocation content by conventional electron backscattering diffraction. Scr. Mater. 58, 994–997. https://doi.org/10.1016/j.scriptamat.2008.01.050

[4] Jiang, J., Britton, T.B., Wilkinson, A.J., 2013. Evolution of dislocation density distributions in copper during tensile deformation. Acta Mater. 61, 7227–7239. https://doi.org/10.1016/j.actamat.2013.08.027
[5] Gutierrez-Urrutia, I., Zaefferer, S., Raabe, D., 2013. Coupling of Electron Channeling with EBSD: Toward the Quantitative Characterization of Deformation Structures in the SEM. JOM 65, 1229–1236. https://doi.org/10.1007/s11837-013-0678-0
[6] Mansour, H., Crimp, M.A., Gey, N., Maloufi, N., 2015. Accurate electron channeling contrast analysis of a low angle sub-grain boundary. Scr. Mater. 109, 76–79. https://doi.org/10.1016/j.scriptamat.2015.07.023
[7] Mansour, H., Guyon, J., Crimp, M.A., Gey, N., Beausir, B., Maloufi, N., 2014. Accurate electron channeling contrast analysis of dislocations in fine grained bulk materials. Scr. Mater. 84–85, 11–14. https://doi.org/10.1016/j.scriptamat.2014.03.001
[8] Oh, J.-S., Yang, C.-W., 2016. Optimal Conditions for Defect Analysis Using Electron Channeling Contrast Imaging. Appl. Microsc. 46, 164–166. https://doi.org/10.9729/AM.2016.46.3.164
[9] Picard, Y.N., Liu, M., Lammatao, J., Kamaladasa, R., De Graef, M., 2014. Theory of dynamical electron channeling contrast images of near-surface crystal defects. Ultramicroscopy 146, 71–78. https://doi.org/10.1016/j.ultramic.2014.07.006
[10] Weidner, A., Martin, S., Klemm, V., Martin, U., Biermann, H., 2011. Stacking faults in high-alloyed metastable austenitic cast steel observed by electron channelling contrast imaging. Scr. Mater. 64, 513–516. https://doi.org/10.1016/j.scriptamat.2010.11.028
[11] Zaefferer, S., Elhami, N.-N., 2014. Theory and application of electron channelling contrast imaging under controlled diffraction conditions. Acta Mater. 75, 20–50. https://doi.org/10.1016/j.actamat.2014.04.018
[12] Ahmed, J., Roberts, S.G., Wilkinson, A.J., 2006. Characterizing dislocation structure evolution during cyclic deformation using electron channelling contrast imaging. Philos. Mag. 86, 4965–4981. https://doi.org/10.1080/14786430600710941
[13] L'hôte, G., Lafond, C., Steyer, P., Deschanel, S., Douillard, T., Langlois, C., Cazottes, S., 2019. Rotational-Electron Channeling Contrast Imaging analysis of dislocation structure in fatigued copper single crystal. Scr. Mater. 162, 103–107. https://doi.org/10.1016/j.scriptamat.2018.10.050
[14] Marx, M., Schaef, W., Welsch, M.T., 2012. The microstructure as crack initiation point and barrier against fatigue damaging. Int. J. Fatigue 41, 57–63. https://doi.org/10.1016/j.ijfatigue.2012.01.018
[15] Herrera, C., Ponge, D., Raabe, D., 2011. Design of a novel Mn-based 1GPa duplex stainless TRIP steel with 60% ductility by a reduction of austenite stability. Acta Mater. 59, 4653–4664. https://doi.org/10.1016/j.actamat.2011.04.011
[16] Ram, F., Li, Z., Zaefferer, S., Hafez Haghighat, S.M., Zhu, Z., Raabe, D., Reed, R.C., 2016. On the origin of creep dislocations in a Ni-base, single-crystal superalloy: an ECCI, EBSD, and dislocation dynamics-based study. Acta Mater. 109, 151–161. https://doi.org/10.1016/j.actamat.2016.02.038
[17] Callahan, P.G., Stinville, J.-C., Yao, E.R., Echlin, M.P., Titus, M.S., De Graef, M., Gianola, D.S., Pollock, T.M., 2018. Transmission scanning electron microscopy: Defect observations and image simulations. Ultramicroscopy 186, 49–61. https://doi.org/10.1016/j.ultramic.2017.11.004

[18] Kessler, P., Orlová, A., 1986. An error of dislocation density evaluation from a micrograph of densely spaced dislocation lines. Mater. Sci. Eng. 82, L1–L5. https://doi.org/10.1016/0025-5416(86)90114-X
[19] David B. Williams, C. Barry Carter, 2009. Transmission Electron Microscopy : A Textbook for Materials Science, 2nd ed. Springer US.
[20] Wilkinson, A.J., Hirsch, P.B., 1995. The effects of surface stress relaxation on electron channelling contrast images of dislocations. Philos. Mag. A 72, 81–103. https://doi.org/10.1080/01418619508239583
[21] Langlois, C., Douillard, T., Yuan, H., Blanchard, N.P., Descamps-Mandine, A., Van de Moortèle, B., Rigotti, C., Epicier, T., 2015. Crystal orientation mapping via ion channeling: An alternative to EBSD. Ultramicroscopy 157, 65–72. https://doi.org/10.1016/j.ultramic.2015.05.023
[22] Lafond, C., Douillard, T., Cazottes, S., Steyer, P., Langlois, C., 2018. Electron CHanneling ORientation Determination (eCHORD): An original approach to crystalline orientation mapping. Ultramicroscopy 186, 146–149. https://doi.org/10.1016/j.ultramic.2017.12.019
[23] Giannuzzi, L.A., Michael, J.R., 2013. Comparison of Channeling Contrast between Ion and Electron Images. Microsc. Microanal. 19, 344–349. https://doi.org/10.1017/S1431927612014286
[24] Joy, D.C., Newbury, D.E., Davidson, D.L., 1982. Electron channeling patterns in the scanning electron microscope. J. Appl. Phys. 53, R81–R122. https://doi.org/10.1063/1.331668
[25] Singh, S., Ram, F., De Graef, M., 2017. EMsoft: open source software for electron diffraction/image simulations. Microsc. Microanal. 23, 212–213. https://doi.org/10.1017/S143192761700174X
[26] Marc De Graef, Michael Jackson, saransh13, wlenthe, Joey Kleingers, Stuart Wright, & josephtessmer. (2019, March 1). EMsoft-org/EMsoft: Release 4.2 to synchronize with DI tutorial paper (Version 4.2). Zenodo. http://doi.org/10.5281/zenodo.2581285
[27] Maetz, J.-Y., Cazottes, S., Verdu, C., Danoix, F., Kléber, X., 2016. Microstructural Evolution in 2101 Lean Duplex Stainless Steel During Low- and Intermediate-Temperature Aging. Microsc. Microanal. 22, 463–473. https://doi.org/10.1017/S1431927616000167
[28] Ross, D.A., Lim, J., Lin, R.-S., Yang, M.-H., 2008. Incremental Learning for Robust Visual Tracking. Int. J. Comput. Vis. 77, 125–141. https://doi.org/10.1007/s11263-007-0075-7
[29] Alsabti, K., Ranka, S., Singh, V., 1997. An efficient k-means clustering algorithm. Electr. Eng. Comput. Sci. 43, 7.
[30] Ester, M., Kriegel, H.-P., Xu, X., Sander, Jörg, 1996. A Density-Based Algorithm for Discovering Clusters in Large Spatial Databases with Noise. KDD Proceeding 96, 226–231.
[31] Pham, M.S., Solenthaler, C., Janssens, K.G.F., Holdsworth, S.R., 2011. Dislocation structure evolution and its effects on cyclic deformation response of AISI 316L stainless steel. Mater. Sci. Eng. A 528, 3261–3269. https://doi.org/10.1016/j.msea.2011.01.015

Acknowledgements:

The project was funded by the BQI 2018 from INSAVALOR (www.insavalor.fr). CLYM (www.clym.fr) is gratefully acknowledged for providing access to the Zeiss NVision SEM/FIB microscope.